Magnetoelectric dual-particulate composites with wasp-waisted magnetic response for broadband energy harvesting

Journal of Alloys and Compounds 783 (2019) 237–245

Contents lists available at ScienceDirect

Journal of Alloys and Compounds

journal homepage: http://www.elsevier.com/locate/jalcom

Magnetoelectric dual-particulate composites with wasp-waisted magnetic response for broadband energy harvesting

Pietro Galizia [a, *], Miguel Algueró [b], Nicolas Bernier [c], Narciso Gambacorti [c], Eleni Aza [d, e], Alexandros Lappas [d], Michel Venet [f], Carmen Galassi [a]

[a] Institute of Science and Technology for Ceramics (CNR-ISTEC), Via Granarolo 64, I-48018, Faenza, RA, Italy
[b] Instituto de Ciencia de Materiales de Madrid (CSIC), 28049, Madrid, Spain
[c] Univ. Grenoble Alpes, CEA, LETI, 38000, Grenoble, France
[d] Institute of Electronic Structure and Laser, Foundation for Research and Technology-Hellas, Vassilika Vouton, Heraklion, 71110, Greece
[e] Department of Materials Science and Engineering, University of Ioannina, 45110, Ioannina, Greece
[f] Departamento de Física, Universidade Federal de São Carlos, 13565-905, São Carlos, SP, Brazil

ARTICLE INFO

Article history:
Received 6 November 2018
Received in revised form
19 December 2018
Accepted 22 December 2018
Available online 24 December 2018

Keywords:
Multiferroic
Multiple parallel twinning
Quite-fast sintering
Isothermal remanence magnetization (IRM)
Irreversible susceptibility
Magnetoelectric diode

ABSTRACT

Dual-particulate composites of cobalt ferrite dispersed in a fully dense PZT matrix are produced by quite-fast sintering of mechanically activated powders. By high-energy milling of the powders a bi-modal grain size distribution, with octahedral nano-grains and larger grains grown by multiple parallel twinning, are achieved in the final microstructure. The material display a "wasp-waisted" magnetic response as a consequence of the two main $CoFe_2O_4$ grain populations and can be exploited for broadband energy harvesting or field sensors. After poling under 5 kV/mm, a maximum d_{33} of 30 pC/N was achieved. This value is an order of magnitude lower than that of bulk PZT. Nevertheless, a magnetoelectric coefficient of 1.74 mV cm^{-1} Oe^{-1} is obtained, which suggests the high potentiality of these materials, since this value is higher than that shown by magnetoelectric composites with similar composition and connectivity reported in literature. This is so for a partially poled material and thus, magnetoelectric coefficients should be significantly increased by improving the poling process.

1. Introduction

The surge of interest in multiferroic materials over the past 15 years has been driven by their fascinating physical properties and huge potential for technological applications, such as sensors, microwave devices, energy harvesting, photovoltaic technologies, solid-state refrigeration, and data storage technologies like multiferroic random access multi-state memories (MFRAM) [1,2]. Outstanding magnetoelectricity has been reported for the multiferroic composites based on piezoelectric and magnetostrictive constituents, which are magnetoelectrically coupled through stress mediation. In particular, remarkable efforts have been done to develop laminated bi-layer and multilayer multiferroic composites as thick or thin films [3,4]. Those structures lead to remarkable magneto-electric coupling coefficients of a few V/(cm·Oe) because in this configuration there are not conductive inclusions into the composite layer and the material can be poled in the conventional way [5,6]. Similar coefficients are expected in the particulate ceramic composites [2]. Their specific strengths are low cost, simple production technology, higher strain mediated magneto-electric coupling (since the density of ferroelectric/ferromagnetic interfaces can be higher) and easy control of electrical and magnetic properties as far as ferroelectric and ferromagnetic phases are mixed in a favourable proportion under the percolation threshold of the ferromagnetic one [7,8]. However, the ferromagnetic phases are often not fully separated within the composite, which produce a local variation of the electric field that can counteract the external one, and even cancel the electric field in ferroelectric portions wrapped by the ferromagnetic phase. Lead zirconate titanate, $Pb(Zr,Ti)O_3$ (PZT), and cobalt ferrite, $CoFe_2O_4$ (CF) are generally chosen as constituents for multiferroic composites owing to their remarkable piezoelectric and magnetostrictive coefficients, respectively. Many papers report the ME properties of said composites and claim that PZT and CF do not react during the sintering process, while not enough attention is given to the densification, possible formation of second phases at interfaces, and the effects of

* Corresponding author.
E-mail address: pietro.galizia@istec.cnr.it (P. Galizia).

https://doi.org/10.1016/j.jallcom.2018.12.273

the porosity on the ME coupling [9,10]. Sentences like: “densely sintered” are often reported with no actual density values being mentioned. A relative density of 97% was achieved by microwave-sintering of PZT-CF (80-20) particulate composites produced by a novel sol-gel route [11]. To achieve higher densification the PbO loss, which can occur at the PZT/CF interfaces even if lead saturated atmosphere is kept constant during the sintering treatment, must be considered. Fully dense PZT-CF (74-26) composites consisting of dispersed cobalt ferrite nanoparticles (250 nm) in PZT matrix were recently produced by quite-fast sintering [12].

In a typical sintering procedure, the heating rate does not exceed 300 °C/h, with a soaking time of more than 30 min, and a cooling rate of less than 5 °C/min. In the quite-fast sintering route described here, a lower sintering temperature is chosen, coupled with a lower soaking time (1 min instead of 120 min), higher heating (>300 °C/h) and cooling (>30 °C/min) rates. This sintering process exploits (i) the faster firing to favour the sintering, and (ii) the lower sintering temperature and soaking time together with the higher cooling rate to reduce the lead volatilization that occurs at temperature higher than 900 °C (where the vapour-phase PbO is not kept at its equilibrium value, as it happens within pores between PZT and CF grains). It is worth highlighting that PbO loss promotes residual porosity in the material, and decreases the piezoelectric and magnetostrictive response of the composite due to the formation of baddeleyite and titania [12] and reaction between titania and CF, respectively [12,13]. The strengths of quite-fast sintering with respect to the high pressure sintering (allows considerable reduction in sintering temperatures [14]), the spark plasma sintering (allows considerable reductions in sintering temperatures and time [15,16]), the two-step sintering (allows reduction in sintering temperatures [17,18]), and the flash sintering (allows considerable reductions in sintering temperatures and time [19–21]) are: no carbon contamination, possibility to supply lead saturated atmosphere, easy control of the process, no overheating, and final homogenous microstructures.

In order to further exploit the faster firing and favour the sintering process, mechanically activated PZT and CF particles can be employed, because it is well known that milled powders display enhanced sinterability [22,23]. In fact, the quite-high heating rate can be expected to trigger the contribution of the high energy stored in the milled particles to promote the sintering, as far as such energy is not released by means of other processes before the densification.

In this work PZT-CF particulate composites with 26 mol% of CF content are produced by quite-fast sintering starting from planetary milled PZT and CF powder mixtures. The focus is placed on the densification process with controlled PbO loss and reactivity of the CF particles with titanium oxide. The final density and the calculated PbO loss (through XRD analysis) are in agreement with the previous work for the specific CF amount selected [12]. The crystal matching between CF and PZT lattices and the absence of second phases at interfaces are checked by TEM analysis, which suggests the good mechanical coupling. The magnetic remanence curves reflect the multimodal CF particle size distribution, which originates in the planetary milling step (added with respect to the previous work [12]) of the PZT-CF mixtures, and suggests the possibility to design dual-particulate composites with a “wasp-waisted” magnetic response for broadband energy harvesting or field sensors. Finally, the magnetoelectric coupling confirms the high potentiality of such particulate composites, despite of partial electrical poling.

2. Material and methods

2.1. Materials preparation

$$0.74Pb_{0.988}(Zr_{0.52}Ti_{0.48})_{0.976}Nb_{0.024}O_3\text{-}0.26CoFe_2O_4 \quad \text{(PZTN-CF)}$$

composites were produced by two-step solid-state-reaction. Firstly, perovskite PZTN and spinel CF powders were prepared separately as described in the previous works [12,22]. Then 0.74PZTN-0.26CF powder mixture was obtained by planetary milling in order to increase the CF dispersion and the reactivity of both phases. The planetary milling, in a stainless steel jar filled to 75 vol% with 1 mm diameter grinding balls and grinding balls/powders mass ratio of 7.7, was performed in pure ethanol at 400 rpm for 10 h. The milled powder mixture was then cold-consolidated into discs of 12 mm diameter by die pressing at 100 MPa, followed by cold isostatic pressing at 300 MPa. The green homogeneous PZTN-CF samples were sintered in a Nannetti Klin FCN 16 furnace controlled using an Ero-Electronic PKP controller. The sintering treatments were performed in lead-saturated atmosphere, at 1100 °C for 1 min. A constant heating flux to reach the sintering temperature in about 25 min (the temperature, T, profile as a function of the time, t, is well fitted by the following equation: $T = -493.5 + 484.6 \ln(t + 1.8)$, where T and t are expressed in °C and min, respectively) was set. Then, the samples were brought back to room temperature by natural cooling of the furnace (the temperature dropped down to 800 °C in 4 min).

2.2. Microstructural characterization

The relative density of the sintered samples was calculated from the density determined by the Archimedes' method normalizing to the theoretical density obtained as the average of PZTN and CF theoretical densities (8.006 g cm^{-3}and 5.304 g cm^{-3}, respectively). The crystalline phases were identified at room temperature by X-Ray Powder Diffraction (XRPD) using a BrukerD8 Advance X-ray diffractometer (θ–θ) with Cu K_α radiation ($\lambda = 1.5418$ Å) and equipped with a LINXEYE detector (Bruker, Karlsruhe, Germany). The scanning range and rate was $15° \leq 2\theta \leq 80°$, and 1.2°/min, respectively. The quantitative determination of the phases was performed with the commercial BRUKER EVA program. The drawings of crystal shape were produced by VESTA software [24]. Morphology, phase compositions, and grain size distribution were investigated by SEM analysis of polished sections performed on a ZEISS SIGMA Field Emission Scanning Electron Microscopy (FE-SEM) system. Image-Pro Analyzer 7.0 software was used to measure the grain size distribution [13]. High-resolution imaging, chemical mapping, and nanodiffraction were carried on in a probe-corrected FEI Titan Themis transmission electron microscope (TEM) operated at 200 kV. Scanning TEM (STEM) images were acquired using the high angle annular dark field (HAADF) detector. Energy dispersive X-ray (EDX) experiments were performed in STEM mode using the four windowless silicon drift detectors (SDD) integrated into the pole piece that allow the X-ray detection over a 0.8 srad solid angle. Nanodiffraction patterns were acquired in precession STEM mode with a precession angle of ~8 mrad and an incident convergence angle of ~2 mrad. The simulation of the electron diffraction patterns was performed in JEMS software [25].

2.3. Magneto-electric characterization

Magnetizing remanence curves were collected with a Quantum Design MPMS XL5 Superconducting Quantum Interference Device (SQUID) magnetometer following the Isothermal Remanence Magnetization (IRM) protocol at 5 K. By following the IRM protocol, the observed magnetic response is less affected by the paramagnetic PZTN phase, and can be completely attributed to the irreversible changes in the magnetic state of the CF [26].

Electrodes were then deposited on the sintered and ground surfaces by screen printing of silver paste and heating at 750 °C for 15 min. The temperature dependence of the dielectric permittivity

and losses was measured between room-temperature (RT) and 500 °C with a HP4284A precision LCR meter. Measurements were dynamically carried out during a heating/cooling cycle with ±1.5 °C/min rate at several frequencies between 100 Hz and 1 MHz.

RT ferroelectric hysteresis loops were recorded under voltage sine waves of increasing amplitude up to 10 kV with a 0.1 Hz frequency, obtained by the combination of a HP 3325B synthesizer/function generator and a TREK 10/40 high-voltage amplifier, while charge was measured with a homebuilt charge to voltage converter and software for loop acquisition and analysis.

Subsequently, the particulate composites were poled for piezoelectric and magnetoelectric characterization. Poling was performed in silicon oil bath under DC field of 5 kV/mm for 30 min, at 120 °C. 24 h after the poling process, the piezoelectric response (d_{33}) was determined by applying a sinusoidal mechanical load of 0.25 N amplitude at 110 Hz with a S 5865 Sinocera d_{33}-m.

Finally, the magnetoelectric response of the composites was characterized. A system comprising a combination of one electromagnet and one Helmholtz coil, designed to independently provide a static magnetic field up to 10 kOe to magnetize the material, and an alternate magnetic field of 30 Oe at 25 Hz (that plays as stimulus) was used, while the magnetoelectric voltage response was monitored with a lock-in amplifier. Both the 3-3 and 3-1 geometries were investigated to obtain the longitudinal and transverse magnetoelectric coefficients α_{33}^{E} and α_{31}^{E}, respectively, as a function of the bias magnetic field *H*, after normalization to the ceramic element thickness.

3. Results and discussion

3.1. Microstructure

Fig. 1 shows the XRPD patterns of a sintered sample. The diffraction peaks are indexed to the cubic spinel structure of $CoFe_2O_4$ (marked with rhombus; for the sake of clarity, only the strongest $I_{CF}(311)$ peak is indexed), and to the tetragonal perovskite structure of PZTN (circles; the strongest peak is $I_{PZTN}(101)$). Traces of undesired baddeleyite, ZrO_2 (for the sake of clarity, only the strongest $I_b(111)$ is marked with a square) are identified. This

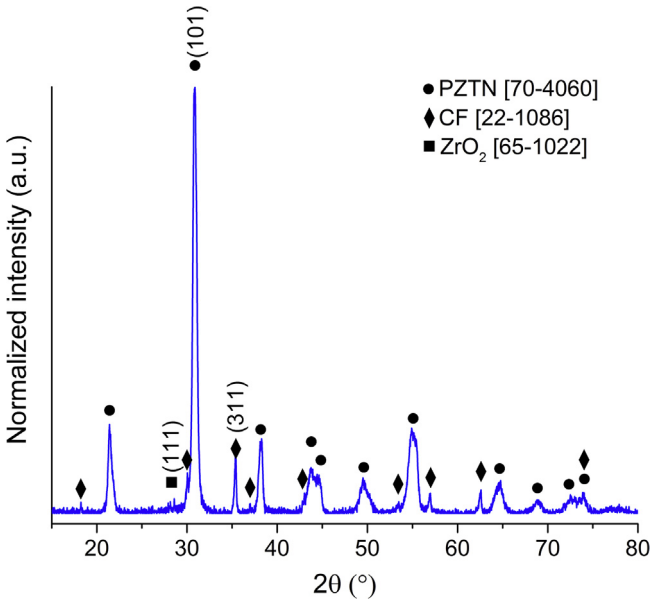

Fig. 1. XRPD spectra of the sintered composite. PDF card numbers of each detected phase are reported in square brackets.

suggests that a small PbO depletion occurs during sintering [12]. The PbO loss of $\delta = 3.7 \pm 0.9$ mol% is calculated through the previously proposed equation [12], and confirms that quite-fast sintering keeps the PbO loss lower than *5%* and thus, leads to a full densification (relative density $\rho\% = 99.1 \pm 0.8\%$). It must be noted that this PbO loss is slightly higher than that of Ref. [12], in spite of achieving higher relative density. This can be ascribed to the milling step performed on the PZTN-CF powders mixture as a result of the higher PZTN/CF interface density, associated with the decreased particles size, increased CF particles dispersion, and enhanced reactivity of the mechanically activated powder.

In Fig. 2 (a) the CF grain size density and frequency distributions (extrapolated by means of SEM image analysis of the polished sections, Fig. 2(b–d)) are shown. The former provides the number of particles per unit volume with radii within the integrated range. The latter makes the peak distribution shape of the larger grains more visible. The sintered composite displays two main CF grain size populations peaked at about 150 nm and 2 μm and characterized by an abundance ratio (number of nanograins on number of micrometric grains) of *3:1*. It means that about the *25%* of CF particles are aggregates, well distributed in the PZTN matrix. In relation of the piezoelectric matrix, the milling step performed on the PZTN-CF powders mixture, along with the shorter sintering time (1 min instead of 30 min) and the higher heating rate (>20 °C/min instead of 6 °C/min) further decreases the PZTN grain size distribution as compared with [12], so that the grain size is reduced from 240 nm down to 150 nm. At low magnification (Fig. 2 (b)) it can be seen that micrometric CF grains are well dispersed and uniformly distributed in a fully dense PZTN matrix. Those large CF grains display the typical octahedral crystal habit of cubic spinel ferrite crystals even if small baddeleyite grains are embedded inside, and some grain boundary is jagged. This confirms that some CF particles remain agglomerated during the planetary milling treatment performed together with the PZTN powder. During sintering, the mechanically activated CF powder (which is characterized by mean particle size lower than 200 nm, and average crystallite size of 13 nm [22]) incorporate PZTN particles, if present, while growing by multiple parallel twinning [22]. At higher magnification (Fig. 2 (c)), it can be seen that a second population of CF grains, characterized by a nanometer size, is present. Also these CF nanograins are characterized by their typical octahedral crystal habit and well facetted faces, and are well dispersed and uniformly distributed. Thus the final microstructure of the composites is based on two different CF grains populations. Furthermore, we can speculate that the CF agglomerates in the green samples are mainly formed by primary CF particles smaller that about 30 nm while the well dispersed particles are bigger than this size. This hypothesis can be supported considering that the smaller the CF particles are (under the single domain limit of about 28 nm) the stronger the tendency to agglomerate (along preferential orientations) is, while the bigger particles remain dispersed as randomly oriented non-interacting particles [27].

In order to understand the crystal growth mechanisms, a brief discussion about the CF grain shape is reported. As said above, both CF grain populations are characterized by the typical octahedral crystal habit of a cubic spinel structure. In fact some grains show a clear octahedral shape more or less slightly truncated by {100} faces. When the shape cannot be easily attributed to a slightly {100}-truncated octahedron, it can be due to a tilt along specific directions (Fig. 3 (a)). Very few grains have a shape that is not attributable to an octahedron, although slightly truncated, i.e. elongated hexagonal projections can be three dimensionally associated to an octahedron with a pronounced {100} truncation (Fig. 3 (c)). The degree of truncation is proportional to the ratio between the growth rate of faces {100} and {111}, which is close to *3* for a

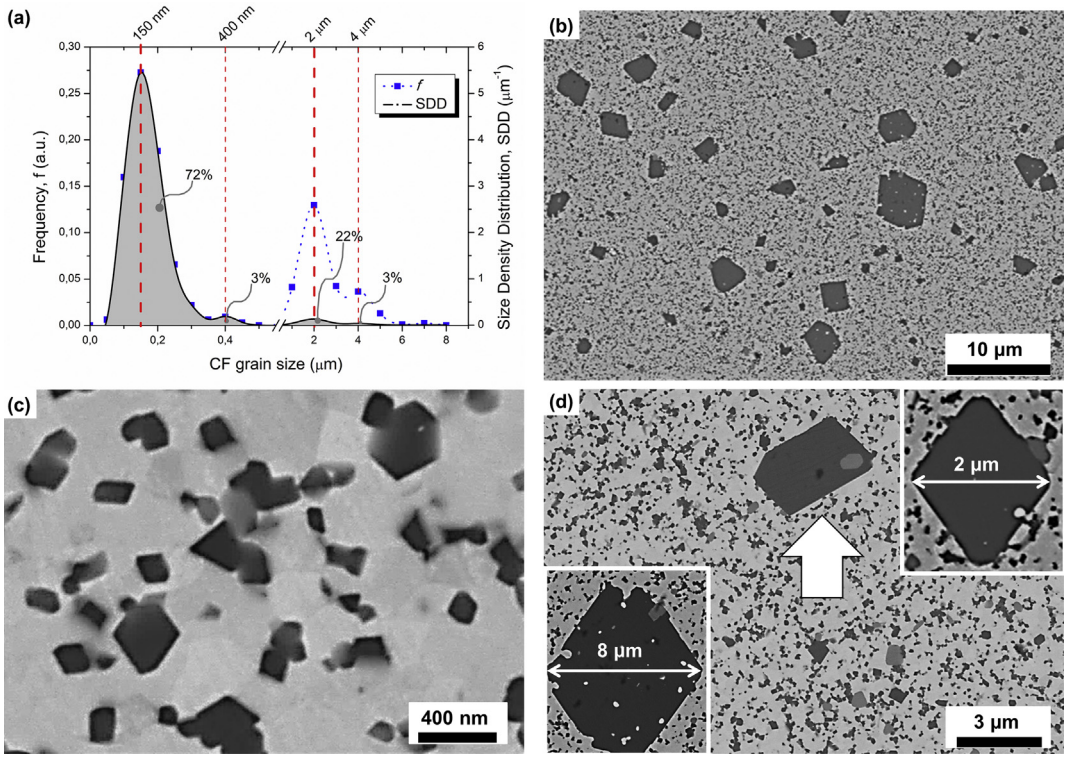

Fig. 2. (a) Frequency distribution of the CF grain size in the sintered sample (square symbols). The right hand ordinates refer to the respective probability distribution functions (solid line, derivatives of splines through the cumulative curve, not shown here). The reported percentages represent the percentage amount of CF grains calculated as integral (grey area). (b–d) Back-scattered SEM images of polished surfaces. The arrow in (d) indicates a CF grain developed by multiple parallel twinning and incorporating a ZrO_2 grain.

truncated octahedron [28]. As the rate of {111} growth can be enhanced by milling [22], we can conclude that almost all CF particles are activated by the planetary milling. Anyway, the shape of nanoparticles is preferentially octahedral which means that the faster growth along <100> results in the disappearance of the {100} facets. Thus the CF nanograins are dominated by the octahedral shape with flat surfaces. As the particles grow larger, if the growth along <110> is faster than in the <100> directions, the CF grains can develop a layered morphology, which can grow along the <111> directions by multiple parallel twinning [22], i.e. the 2D rectangular and trapezoidal shapes (Fig. 2 (b) and (d)) correspond to the projections of a lamella developed on a (111) face. In particular the 2D shape of the pointed CF grains in Fig. 2 (d) – the one with baddeleyite incorporated – corresponds to the projection along the [110] direction of a layered grain on a (111) face and developed by multiple parallel twinning along the [111] direction (Fig. 3 (b)).

The correspondence between the projection shape and the expected crystal structure is proved by the agreement between experimental and simulated electron diffraction pattern obtained in the TEM analysis (Fig. 4 (a) and (b)). In particular, it can be seen that the projection shape of the nanograin and micrograin corresponds to the <112> and <110> project direction of a {100}-truncated octahedron and {100}-truncated {111}-lamella, respectively. For both grains, the indexing of the diffraction pattern confirmed the presence of the $CoFe_2O_4$ phase (CIF file #1535820). Furthermore, the EDS mapping (Fig. 4 (c)) confirms the CF grains embedded in the PZTN matrix and the precipitation of ZrO_2 and $PbTiO_3$ as expected owing to the PbO loss [12].

Although some Pb depletion has occurred, the STEM-HAADF image shows continuous and sharp CF/PZTN interfaces (i.e. with the heavy atoms regularly located along the interface) for both the CF micrograin and nanograin (Fig. 5 (a)). Only low strain value (close to the sensitivity of the characterization technique) of the order of *0.2%* are measured at the CF/PZTN interfaces. This result confirms that the quite-fast sintering of the PZTN-CF system can let to achieve the predicted magnetoelectric response by limiting the misfit strain at the interface, and the interdiffusion and/or chemical reactions between the two phases [3]. Indeed these results demonstrate the absence of any interfacial second phase between the two ferroic phases, and the good mechanical coupling between them. It is worth noting that ZrO_2 grains embedded in the CF micrograin display interface with a clear orientation relationship without any evidence of a change of lattice parameters across the interface (Fig. 5 (b)). This confirms that CF can promote the PbO loss by stabilizing the baddeleyite phase.

3.2. Magneto-electric properties

Even if the different grain shapes (nanograins have octahedral morphology while micrometric grains can be octahedral multiple parallel twinned along <111> directions or just a stack of multiple parallel twinned (111)-lamellae) and the different interfaces (CF/PZTN, CF/$PbTiO_3$, CF/ZrO_2) affect the magnetic coercivity and susceptibility of the CF [22,29–31], the main extrinsic parameters are the grain size and strain [27]. In fact, it is well known that CF displays a strongly different magnetic behaviour depending on its grain size [12,32,33]. Since the strain can be considered insignificant (lower than *0.2%*), the magnetic response should be mainly controlled by the CF grain size distribution, which is bimodal. Indeed, a differentiated magnetic response is found looking at the irreversible susceptibility, χ_{irr}, the first derivative of the remanence curve, M_{irr} (Fig. 6). χ_{irr} reflects real variations in the distribution of coercivities and hence can be correlated with the CF grain size distribution. Examination of the parameters derived from

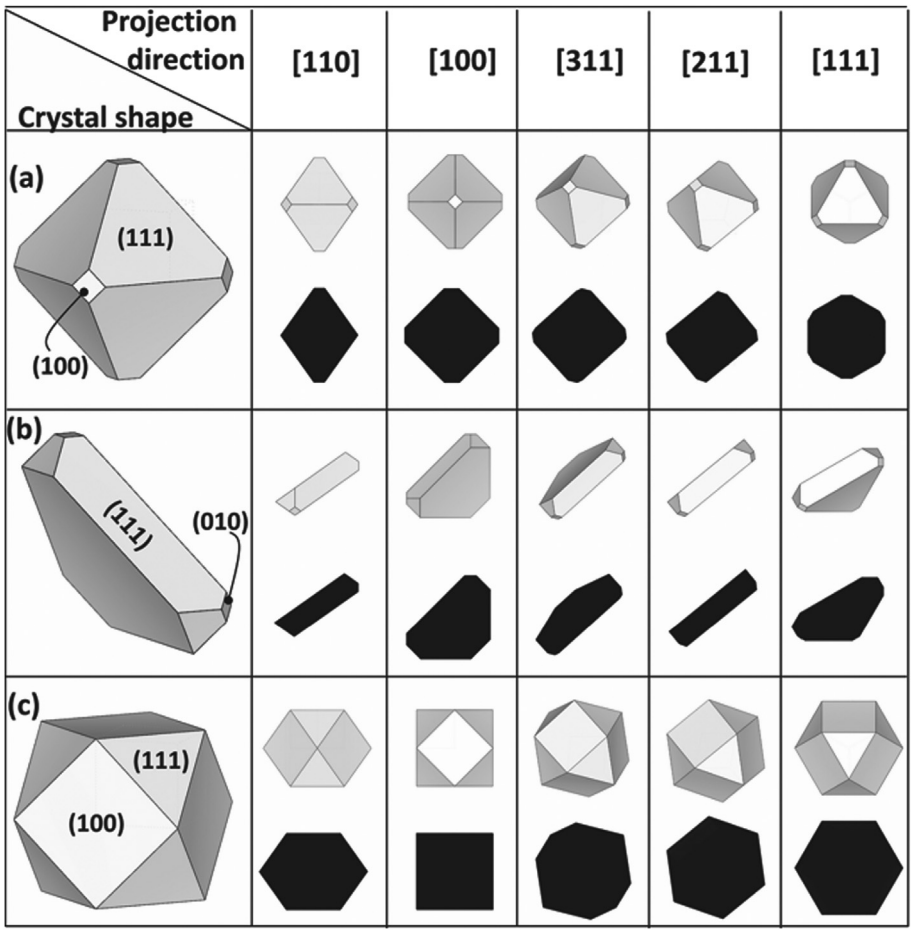

Fig. 3. and 2 D exploitation of (a) slightly {100}-truncated octahedron, (b) slightly {100}-truncated {111}-lamella (c) {100}-truncated-octahedron along main projection directions.

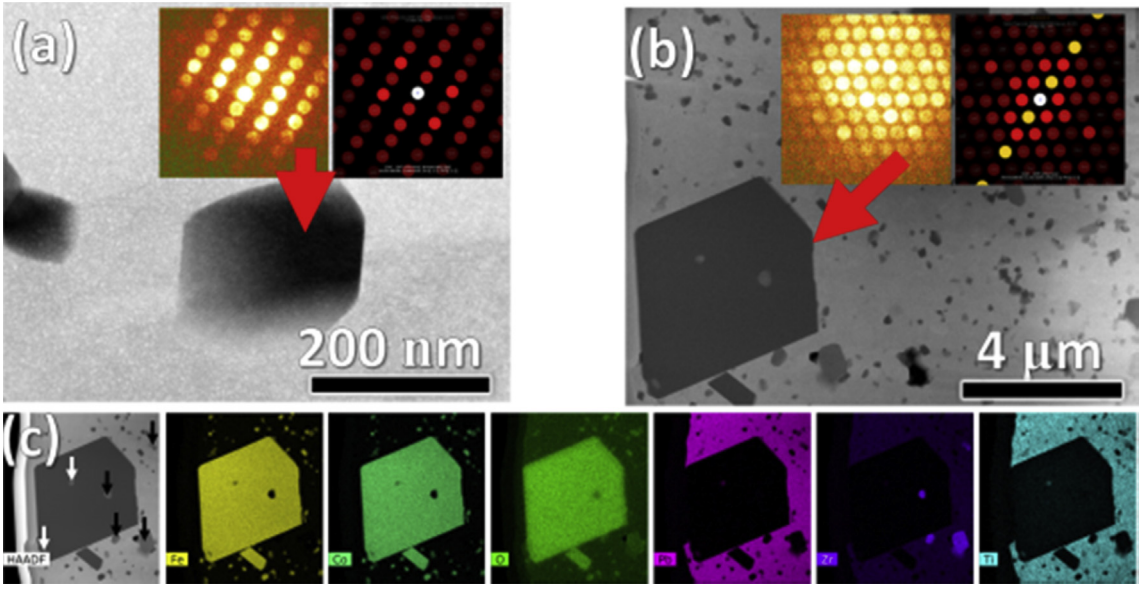

Fig. 4. A representative electron diffraction pattern acquired on the CF (a) nanograin and (b) macrigrain. In the inset the experimental and simulated diffraction pattern obtained with the zone axis <110> and <211> for the nanograin and micrograin, respectively. (c) Chemical mapping by energy dispersive spectroscopy (EDS). In the STEM-HAADF image (the first on the left) ZrO_2 and $PbTiO_3$ grains are pointed by black and white arrows, respectively. Then, from left to right, the spatial distribution of Fe, Co, O, Pb, Zr, and Ti.

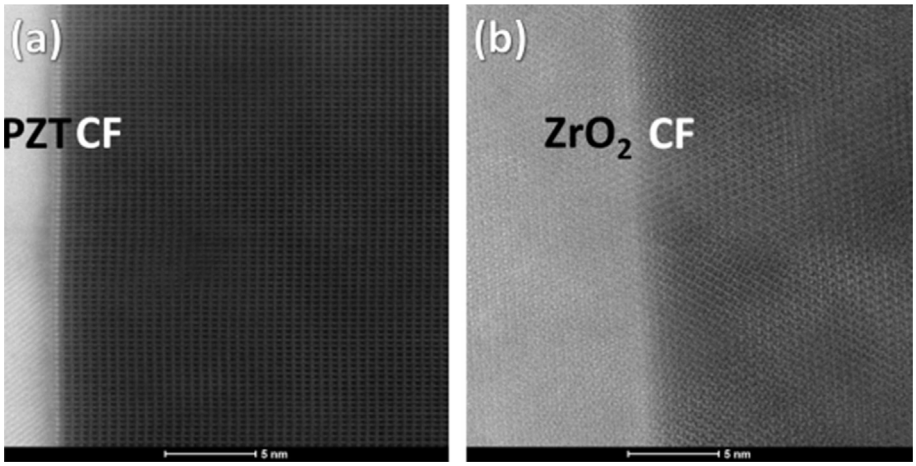

Fig. 5. High-resolution STEM-HAADF image of (a) PZTN/CF and (b) ZrO_2/CF interfaces.

remanence curve indicates that 72% of the irreversible magnetization is given by two different "soft" CF populations, whose irreversible susceptibility peaks (χ_{irr}) are centred at *5.4* kOe and *9.5* kOe χ_{irr} peak of the "hard" CF occurs at *17.4* kOe and accounts for the remaining 28% of the total magnetic moment. The latter coercivity value is comparable to that of single domain limit CF particles [27] and the large broadening, *10.4* kOe, of the switching field distribution is in agreement with the expected wide coercivity distribution of particles with a size around the single domain limit. Hence, the developed PZTN-CF microstructures is a dual-particulate composite since the dispersed CF results in two different phases (soft ferromagnetic phase + hard ferromagnetic phase), for which there are two well differentiated magnetic responses. This behaviour has been referred to as "wasp-waisted" magnetic characteristics [34], and suggests the possibility to develop dual-particulate magnetoelectric composites with a wider and differentiated magnetic sensitivity that could be exploited for broadband energy harvesting, and novel sensing applications. The currently developed ME devices for the energy harvesting consist in a cantilever structure, working at the resonance frequency; so far it maximizes the magneto-mechano-electric interactions and transforms the magnetic noise field in an energy source [35]. According to this configuration, the two magnetic phases, by resonating at two distinct frequencies, extend the working range and could increase the efficiency [36].

Electrical poling was controlled by measuring the piezoelectric

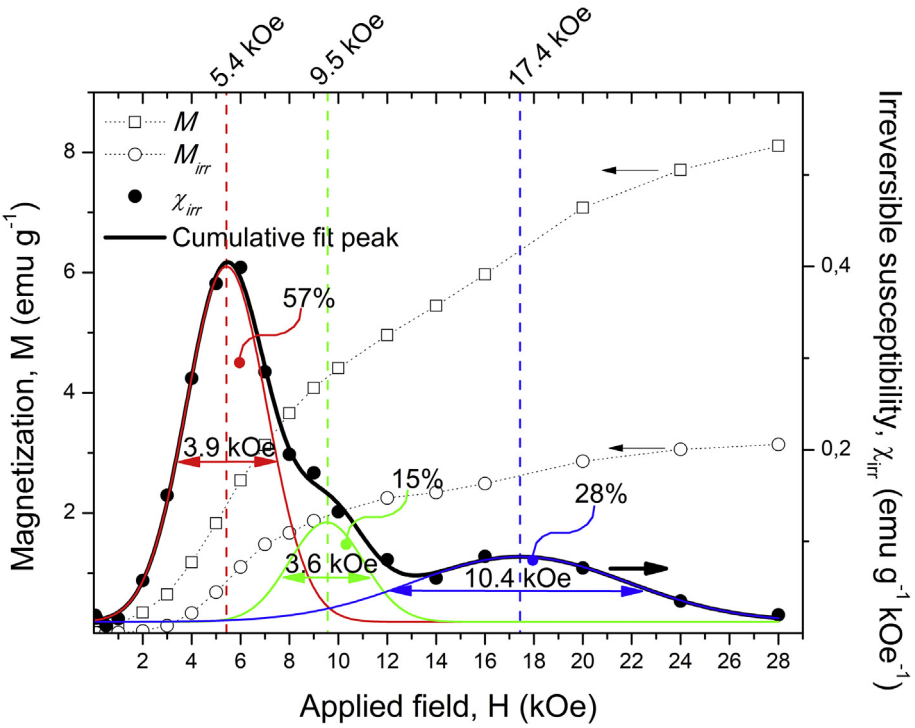

Fig. 6. Magnetization (M, empty square symbols) and remanence (M_{irr}, empty circle symbols) curves at *5 K*. The right hand ordinate refers to the irreversible susceptibility (the first derivative of the remanence curve, $\chi_{irr} = dM_{irr}/dH$, solid symbols). χ_{irr} is deconvoluted into three Gaussian peaks and the cumulative fit peak is shown as the black continuous line (Statistics: $R^2 = 0.995$; reduced chi-squared = $7.817 \cdot 10^{-11}$). For each deconvoluted peak, the value of the full-width-at-half-height, the centre, and the area fraction percentage are reported.

response of the sample by means of the Berlincourt d_{33} piezometer. A d_{33} piezoelectric coefficient of *30 pC N*$^{-1}$ was found, which is one order of magnitude lower than values around *340 pC N*$^{-1}$ reported for soft Nb-doped PZT with an average grain size of 180 nm [37]. The low piezoelectric activity is most probably associated with partial poling that was already anticipated by non-saturated hysteresis loops shown in Fig. 7 (a). Note the non-negligible conduction contribution and that only incipient switching was attained at a field as high as 6 kV/mm. Non-saturated hysteresis loops are typical for particulate composite ceramics due to the presence of non-ferroelectric phase [38]. The content of cobalt ferrite is far from the percolation threshold, otherwise it would not be possible to apply 6 kV/mm due to the eddy current of the CF. The effect of the finite conductivity of CF is apparent not only in the hysteresis loops, but also in the dielectric permittivity. This is shown in Fig. 7 (b) and (c), where conduction is responsible for the frequency dispersion and its exponential increase at high temperatures. It is worth noticing that, even if only partial poling was achieved, the piezoelectric coefficient obtained in the fully densified composite is about ten times higher than that obtained with porous particulate composite ceramics with similar composition [38]. Future strategies should be adopted in order to get a full poling. For example: (i) by trying to increase the PZT grain size, for example by adding a certain fraction of coarse PZT particles. In this way these particles should promote the Ostwald ripening and hence increase the grain size. (ii) By optimizing the temperature of the poling process in order to find the best compromise between the ferroelectric domains mobility and the amount of charge carriers of the CF. (iii) By tailoring the PSD of CF and its spatial distribution to reduce the total conductivity of the composite. (iv) Or, eventually, by reducing the amount of CF which acts also as grain refiner of the PZT grains.

The voltage magnetoelectric coupling coefficients are shown in Fig. 7 (d). Larger coefficients were obtained in the 3-3 magnetoelectric geometry than in the 3-1 one as expected for a particulate composite. The maximum α_{33}^{E} value of *1.74* mV cm^{-1} Oe^{-1}is higher than that shown by similar composites with a lower density (*1.56* mV cm^{-1} Oe^{-1} [11]), even if the full poling was not achieved. Anyway, the obtained value is still too low, if compared with the theoretical one which is three orders of magnitude higher [3], and further efforts are necessary to increase the poling and approach the theoretical ME value. Finally, note the large difference between the magnetoelectric response under positive and negative bias magnetic fields, relevant for α_{31}^{E}. This is an unexpected result that somehow resembles the current *vs.* voltage response of an ideal *p-n* diode. In fact, according to α_{31}-*H* characteristic (Fig. 7 (d)), an external AC magnetic field, placed across the ME diode, can result, or cannot result, in a built-in potential, depending of the sign of the magnetizing field ($\alpha_{31} > 0$, or $\alpha_{31} = 0$, respectively). Hence, the understanding of this phenomenon might lead to develop advanced magnetoelectric diodes.

We think that the combination of two or more ferromagnetic phases, as well as ferroelectric phases, paves the way for the development of insightful, opinionated, and even visionary new types of electronics. The exploitation of different magnetic irreversible susceptibilities, as presented in this article, or even opposed magnetocrystalline anisotropy, as it was published in Ref. [39], when the present work was already submitted, are the two first examples of this emerging approach for the development of cutting-edge technologies.

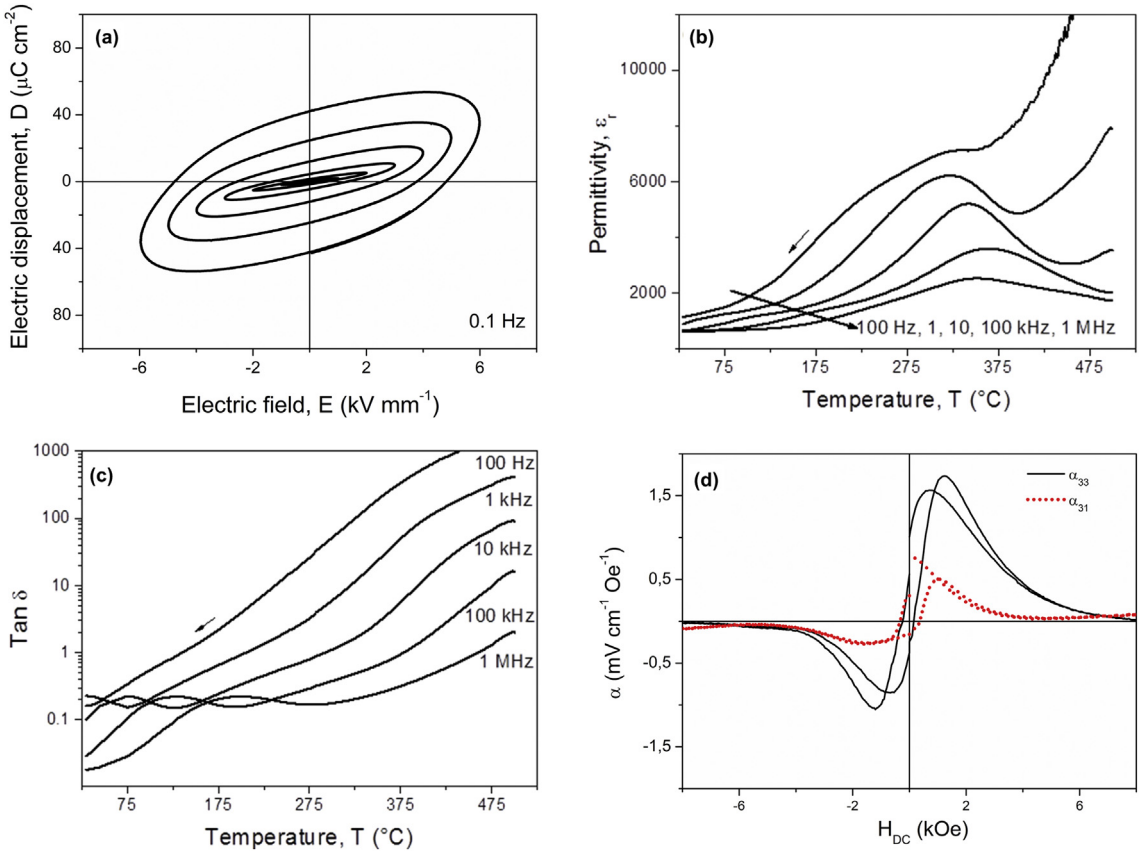

Fig. 7. (a) Ferroelectric hysteresis loops. (b) Permittivity, ε_r, and (c) dielectric loss, tan δ as a function of temperature, *T*, and frequency. (d) Magnetoelectric coupling coefficients *vs.* applied magnetic field.

4. Conclusions

Fully dense PZT-cobalt ferrite dual-particulate composites can be produced by quite-fast sintering of mechanically activated powder mixtures. This process is the successful response to the challenges of the different shrinkage rates, thermal expansion mismatch, and interface inhomogeneities displayed by particulate composites. The milling step of Nb-doped PZT-cobalt ferrite powder mixture seems to increase the relative density in spite of the PbO loss as a result of the increased particle reactivity and higher Nb-doped PZT/cobalt ferrite interfaces density. The microstructure of the dual-particulate composites consisted in two cobalt ferrite grain size populations dispersed in the Nb-doped PZT matrix. Planetary milling is the key process step to produce the PZT-CF dual-particulate composites since it is shown that: (i) high-energy milling boosts the growth rate of {111} faces with respect to {100} ones, and allows the growth by multiple parallel twinning. Since the two cobalt ferrite populations are quite different from each other as one consists of single octahedral grain of 150 nm, and the other is multiple parallel twinned grains of 2 μm, a "wasp-waisted" magnetic behaviour is displayed. The remanence curve shows that *28%* of the magnetic moment is given by single domain limit particles. The material subjected to a poling process under 5 kV/mm did not attain full saturation, so that the maximum d_{33} is an order of magnitude lower than that of the fully saturated bulk matrix. Nevertheless, the obtained magnetoelectric coupling of *1.74* mV cm^{-1} Oe^{-1} is higher than that reported in literature for similar composites.

Acknowledgements

PG acknowledges the contribution of the Nanoscience Foundries and Fine Analysis (NFFA) European Research Infrastructure. In fact, this project has received funding from the EU-H2020 research and innovation programme under grant agreement No 654360 having benefitted from the access provided by Laboratoire d'électronique des technologies de l'information (CEA-LETI) in Grenoble and Foundation for Research and Technology - Hellas (FORTH) in Heraklion within the framework of the NFFA-Europe Transnational Access Activity. Guillaume Audoit (CEA-LETI) and Audrey Jannaud (SERMA Technologies) are gratefully acknowledged for the preparation of the sample for TEM analysis. NB and NG acknowledge the "Recherches Technologiques de Base" Program of the French Ministry of Research which has supported the NanoCharacterisation PlatForm (PFNC). MA also acknowledges funding by Spanish MINECO (projects MAT2014-58816-R and MAT2017-88788-R).

References

[1] M.M. Vopson, Fundamentals of multiferroic materials, their possible applications, Crit. Rev. Solid State Mater. Sci. 4 (2015) 223–250.
[2] C.-W. Nan, M.I. Bichurin, S.X. Dong, D. Viehland, G. Srinivasan, Multiferroic magnetoelectric composites: historical perspective, status, and future directions, J. Appl. Phys. 103 (2008), 031101, https://doi.org/10.1063/1.2836410.
[3] H. Palneedi, V. Annapureddy, S. Priya, J. Ryu, Status and perspectives of multiferroic magnetoelectric composite materials and applications, Actuators 5 (2016) 9, https://doi.org/10.3390/act5010009.
[4] G. Schileo, C. Pascual-Gonzalez, M. Alguero, I.M. Reaney, P. Postolach, L. Mitoseriu, K. Reichmann, M. Venet, A. Feteir, Multiferroic and magnetoelectric properties of $Pb_{0.99}[Zr_{0.45}Ti_{0.47}(Ni_{1/3}Sb_{2/3})_{0.08}]O_3$–$CoFe_2O_4$ multilayer composites fabricated by tape casting, J. Eur. Ceram. Soc. 38 (2018) 1473–1478, https://doi.org/10.1016/j.jeurceramsoc.2017.10.055.
[5] M. Khodaei, A. Eshghinejad, S.A. Seyyed Ebrahimi, S. Baik, Nanoscale magnetoelectric coupling study in (111)-oriented PZT-Co ferrite multiferroic nanobilayer thin film using piezo response force microscopy: effect of Co ferrite composition, Sens. Actuators, A 242 (2016) 92–98, https://doi.org/10.1016/j.sna.2016.02.041.
[6] P. Galizia, I.V. Ciuchi, D. Gardini, C. Baldisserri, C. Galassi, Bilayer thick structures based on $CoFe_2O_4/TiO_2$ composite and niobium-doped PZT obtained by electrophoretic deposition, J. Eur. Ceram. Soc. 36 (2016) 373–380, https://doi.org/10.1016/j.jeurceramsoc.2015.07.038.
[7] Y. Koutsawa, F. Biscani, S. Belouettar, H. Nasser, E. Carrera, Toward micromechanics of coupled fields materials containing functionally graded inhomogeneities: multi-coating approach, Mech. Adv. Mater. Struct. 18 (2011) 524–530, https://doi.org/10.1080/15376494.2011.605010.
[8] B. Patel, T.I. Zohdi, Numerical estimation of effective electromagnetic properties for design of particulate composites, Mater. Des. 94 (2016) 546–553, https://doi.org/10.1016/j.matdes.2016.01.015.
[9] J.H. Peng, M. Hojamberdiev, H.Q. Li, D.L. Mao, Y.-J. Zhao, P. Liu, J.P. Zhou, G.Q. Zhu, Electrical, magnetic, and direct and converse magneto-electric properties of (1-x)$Pb(Zr_{0.52}Ti_{0.48})O_3$-(x)$CoFe_2O_4$ (PZT-CFO) magneto-electric composites, J. Magn. Magn. Mater. 378 (2015) 298–305, https://doi.org/10.101/j.jmmm.2014.11.060.
[10] A. Sakanas, D. Nuzhnyy, R. Grigalaitis, J. Banys, F. Borodavka, S. Kamba, C.E. Ciomaga, L. Mitoseriu, Dielectric and phonon spectroscopy of Nb-doped $Pb(Zr_{1-y}Ti_y)O_3$-$CoFe_2O_4$ composites, J. Appl. Phys. 121 (2017), 214101.
[11] C.P. Fernández, F.L. Zabotto, D. Garcia, R.H. Kiminami, In situ sol-gel co-synthesis under controlled pH and microwave sintering of PZT/$CoFe_2O_4$ magnetoelectric composite ceramics, Ceram. Int. 42 (2016) 3239–3249, https://doi.org/10.1016/j.ceramint.2015.10.115.
[12] P. Galizia, C.E. Ciomaga, L. Mitoseriu, C. Galassi, PZT-cobalt ferrite particulate composites: densification and lead loss controlled by quite-fast sintering, J. Eur. Ceram. Soc. 37 (2017) 161–168, https://doi.org/10.1016/j.jeurceramsoc.2016.08.025.
[13] P. Galizia, C. Baldisserri, C. Galassi, Microstructure development in novel titania-cobalt ferrite ceramic materials, Ceram. Int. 42 (2016) 2634–2641, https://doi.org/10.1016/j.ceramint.2015.10.069.
[14] C. Ponzoni, M. Cannio, R. Rosa, T. Chudoba, E. Pietrzykowka, V. Buscaglia, E. Finocchio, P. Nanni, W. Łojkowski, C. Leonelli, Effect of low-temperature high-pressure sintering on $BiFeO_3$ density, electrical magnetic and structural properties, Phase Transitions 86 (2013) 1104–1114, https://doi.org/10.1080/01411594.2013.771738.
[15] F. Maglia, U. Anselmi-Tamburini, G. Chiodelli, H.E. Çamurlu, M. Dapiaggi, Z.A. Munir, Electrical, structural, and microstructural characterization of nanometric $La_{0.9}Sr_{0.1}Ga_{0.8}Mg_{0.2}O_{3-\delta}$ (LSGM) prepared by high-pressure spark plasma sintering, Solid State Ionics 180 (2009) 36–40, https://doi.org/10.1016/j.ssi.2008.10.005.
[16] H. Amorín, J. Ricote, I. San-Felipe, N. Salazar, R. Del Campo, Y. Romaguera-Barcelay, J. Pérez de la Cruz, P. Ramos, E. Vila, A. Castro, M. Algueró, Multilayer ceramic magnetoelectric composites with tailored interfaces for enhanced response, ACS Appl. Mater. Interfaces 9 (2017) 39094–39104, https://doi.org/10.1021/acsami.7b14775.
[17] X.X. Li, J.J. Zhou, J.X. Deng, H. Zheng, L. Zheng, P. Zheng, H.B. Qin, Synthesis of dense, fine-grained YIG ceramics by two-step sintering, J. Electron. Mater. 45 (2016) 4973–4978, https://doi.org/10.1007/s11664-016-4690-3.
[18] X.-H. Wang, X.-Y. Deng, H.-L. Bai, H. Zhou, W.-G. Qu, L.-T. Li, Two-step sintering of ceramics with constant grain-size, II: $BaTiO_3$ and Ni-Cu-Zn ferrite, J. Am. Ceram. Soc. 89 (2006) 438–443, https://doi.org/10.1111/j.1551-2916.2005.00728.x.
[19] M. Cologna, J.S. Francis, R. Raj, Field assisted and flash sintering of alumina and its relationship to conductivity and MgO-doping, J. Eur. Ceram. Soc. 31 (2011) 2827–2837, https://doi.org/10.1016/j.jeurceramsoc.2011.07.004.
[20] S. Grasso, Y. Sakka, N. Rendtorff, C. Hu, G. Maizza, H. Borodianska, O. Vasylkiv, Modeling of the temperature distribution of flash sintered zirconia, J. Ceram. Soc. Jpn. 119 (2011) 144–146.
[21] R.I. Todd, E. Zapata-Solvas, R.S. Bonilla, T. Sneddon, P.R. Wilshaw, Electrical characteristics of flash sintering: thermal runaway of Joule heating, J. Eur. Ceram. Soc. 35 (2015) 1865–1877, https://doi.org/10.1016/j.jeurceramsoc.2014.12.022.
[22] P. Galizia, C. Baldisserri, C. Capiani, C. Galassi, Multiple parallel twinning overgrowth in nanostructured dense cobalt ferrite, Mater. Des. 109 (2016) 19–26, https://doi.org/10.1016/j.matdes.2016.07.050.
[23] H. Maiwa, O. Kimura, K. Shoji, H. Ochiai, Low temperature sintering of PZT ceramics without additives via an ordinary ceramic route, J. Eur. Ceram. Soc. 25 (2005) 2383–2385, https://doi.org/10.1016/j.jeurceramsoc.2005.03.066.
[24] K. Momma, F. Izumi, VESTA 3 for three-dimensional visualization of crystal, volumetric and morphology data, J. Appl. Crystallogr. 44 (2011) 1272–1276.
[25] J.-P. Morniroli, P. Stadelmann, G. Ji, S. Nicolopoulos, The symmetry of precession electron diffraction patterns, J. Microsc. 237 (2010) 511–515, https://doi.org/10.1111/j.1365-2818.2009.03311.x.
[26] P.I. Mayo, K. O'Grady, R.W. Chantrell, J.A. Cambridge, I.L. Sanders, T. Yogi, J.K. Howard, Magnetic measurement of interaction effects in CoNiCr and CoPtCr thin film media, J. Magn. Magn. Mater. 95 (1991) 109–117.
[27] P. Galizia, M. Cernea, V. Mihalache, L. Diamandescu, G. Maizza, C. Galassi, Easy batch-scale production of cobalt ferrite nanopowders by two-step milling: structural and magnetic characterization, Mater. Des. 130 (2017) 327–335, https://doi.org/10.1016/j.matdes.2017.05.062.
[28] A.-L. Lopes-Moriyama, V. Madigou, C. Pereira de Souza, C. Leroux, Controlled synthesis of $CoFe_2O_4$ nano-octahedra, Powder Technol. 256 (2014) 482–489, https://doi.org/10.1016/j.powtec.2014.01.080.
[29] A. López-Ortega, E. Lottini, C. de Julián Fernández, C. Sangregorio, Exploring the magnetic properties of cobalt-ferrite nanoparticles for the development of a rare earth-free permanent magnet, Chem. Mater. 27 (2015) 4048–4056, https://doi.org/10.1021/acs.chemmater.5b01034.
[30] M.V. Limaye, S.B. Singh, S.K. Date, D. Kothari, V. Raghavendra Reddy, A. Gupta, V. Sathe, R. Jane Choudhary, S.K. Kulkarni, High coercivity of oleic acid capped

$CoFe_2O_4$ nanoparticles at room temperature, J. Phys. Chem. B 113 (2009) 9070–9076, https://doi.org/10.1021/jp810975v.
[31] L. Yan, Y. Wang, J. Li, A. Pyatakov, D. Viehland, Nanogrowth twins and abnormal magnetic behaviour in $CoFe_2O_4$ epitaxial thin films, J. Appl. Phys. 104 (2008), 123910, https://doi.org/10.1063/1.3033371.
[32] D. Carta, M.F. Casula, A. Falqui, D. Loche, G. Mountjoy, C. Sangregorio, A. Corrias, A structural and magnetic investigation of the inversion degree in ferrite nanocrystals MFe_2O_4 (M = Mn, Co, Ni), J. Phys. Chem. C 113 (2009) 8606–8615, https://doi.org/10.1021/jp901077c.
[33] S. Diodati, L. Pandolfo, A. Caneschi, S. Gialanella, S. Gross, Green and low temperature synthesis of nano-crystalline transition metal ferrites by simple wet chemistry routes, Nano Res. 7 (2014) 1027–1042, https://doi.org/10.1007/s12274-014-0466-3.
[34] O. Condurache, I. Turcan, L. Curecheriu, C.E. Ciomaga, P. Postolache, G. Ciobanu, L. Mitoseriu, Towards novel functional properties by interface reaction in mixtures of $BaTiO_3$-Fe_2O_3 composite ceramics, Ceram. Int. 43 (2017) 1098–1105.
[35] Y. Cheng, B. Peng, Z. Hu, Z. Zhou, M. Liu, Recent development and status of magnetoelectric materials and devices, Phys. Lett. 382 (2018) 3018–3025.
[36] G. Srinivasan, Magnetoelectric composites, Annu. Rev. Mater. Res. 40 (2010) 153–178.
[37] C.A. Randall, N. Kim, J.-P. Kucera, W. Cao, T.R. Shrout, Intrinsic and extrinsic size effects in fine-grained morphotropic phase boundary lead zirconate titanate ceramics, J. Am. Ceram. Soc. 81 (1998) 677–688.
[38] J.D. Bobić, M. Ivanov, N.I. Ilić, A.S. Dzunuzović, M.M. Vijatović Petrović, J. Banys, A. Ribic, Z. Despotovic, B.D. Stojanovic, PZT-nickel ferrite and PZT-cobalt ferrite comparative study: structural, dielectric, ferroelectric and magnetic properties of composite ceramics, Ceram. Int. 44 (2018) 6551–6557.
[39] Y. Yan, L.D. Geng, Y. Tan, J. Ma, L. Zhang, M. Sanghadasa, K. Ngo, A.W. Ghosh, Y.U. Wang, S. Priya, Colossal tunability in high frequency magnetoelectric voltage tunable inductors, Nat. Commun. 9 (2018) 4998.